Nanorobots-Assisted Natural Computation for Multifocal Tumor Sensitization and Targeting

Shaolong Shi, *Member, IEEE*, Yizhen Yan, Junfeng Xiong, *Student Member, IEEE*, U Kei Cheang, *Member, IEEE*, Xin Yao, *Fellow, IEEE*, and Yifan Chen, *Senior Member, IEEE*

***Abstract*— We have proposed a new tumor sensitization and targeting (TST) framework, named *in vivo* computation, in our previous investigations. The problem of TST for an early and microscopic tumor is interpreted from the computational perspective with nanorobots being the "natural" computing agents, the high-risk tissue being the search space, the tumor targeted being the global optimal solution, and the tumor-triggered biological gradient field (BGF) providing the aided knowledge for fitness evaluation of nanorobots. This natural computation process can be seen as on-the-fly path planning for nanorobot swarms with an unknown target position, which is different from the traditional path planning methods. Our previous works are focusing on the TST for a solitary lesion, where we proposed the weak priority evolution strategy (WP-ES) to adapt to the actuating mode of the homogeneous magnetic field used in the state-of-the-art nanorobotic platforms, and some *in vitro* validations were performed. In this paper, we focus on the problem of TST for multifocal tumors, which can be seen as a multimodal optimization problem for the "natural" computation. To overcome this issue, we propose a sequential targeting strategy (Se-TS) to complete TST for the multiple lesions with the assistance of nanorobot swarms, which are maneuvered by the external actuating and tracking devices according to the WP-ES. The Se-TS is used to modify the BGF landscape after a tumor is detected by a nanorobot swarm with the gathered BGF information around the detected tumor. Next, another nanorobot swarm will be employed to find the second tumor according to the modified BGF landscape without being misguided to the previous one. In this way, all the tumor lesions will be detected one by one. In other words, the paths of nanorobots to find the targets can be generated successively with the sequential modification of the BGF landscape. To demonstrate the effectiveness of the proposed Se-TS, we perform comprehensive simulation studies by enhancing the WP-ES based swarm intelligence algorithms using this strategy considering the realistic in-body constraints. The performance is compared against that of the "brute-force" search, which corresponds to the traditional systemic tumor targeting, and also against that of the standard swarm intelligence algorithms from the algorithmic perspective. Furthermore, some *in vitro* experiments are performed by using Janus microparticles as magnetic nanorobots, a two-dimensional microchannel network as the human vasculature, and a magnetic nanorobotic control system as the external actuating and tracking system. Results from the *in silico* simulations and *in vitro* experiments verify the effectiveness of the proposed Se-TS for two representative BGF landscapes.**

***Index Terms*— Natural computation, nanorobots, swarm intelligence, tumor sensitization and targeting, magnetic field control.**

Manuscript received August 4, 2020; revised November 29, 2020; accepted November 30, 2020. Date of publication December 3, 2020; date of current version April 1, 2021. This work was supported in part by the Guangdong Provincial Key Laboratory under Grant 2020B121201001, in part by the Program for Guangdong Introducing Innovative and Entrepreneurial Teams under Grant 2017ZT07X386, in part by the Shenzhen Science and Technology Program under Grant KQTD2016112514355531, in part by the National Natural Science Foundation of China (NSFC) under Grant 51850410516, in part by the Science and Technology Innovation Committee Foundation of Shenzhen under Grant JCYJ20180302174151692, and in part by the Shenzhen Municipal Government, Peacock Plan, under Grant 20181119590C. *(Corresponding author: Yifan Chen.)*

Shaolong Shi is with the School of Life Science and Technology, University of Electronic Science and Technology of China, Chengdu 611731, China.

Yizhen Yan is with the Max Planck Partner Institute for Computational Biology, Chinese Academy of Sciences, Shanghai 100864, China.

Junfeng Xiong and U Kei Cheang are with the Department of Mechanical and Energy Engineering, Southern University of Science and Technology, Shenzhen 518055, China.

Xin Yao is with the Guangdong Provincial Key Laboratory of Brain-Inspired Intelligent Computation, Department of Computer Science and Engineering, Southern University of Science and Technology, Shenzhen 518055, China.

Yifan Chen is with the School of Life Science and Technology, University of Electronic Science and Technology of China, Chengdu 611731, China, and also with the Division of Health, Engineering, Computing and Science, University of Waikato, Hamilton 3216, New Zealand (e-mail: yifan.chen@uestc.edu.cn).

This article has supplementary downloadable material available at https://doi.org/10.1109/TNB.2020.3042266, provided by the authors.

Digital Object Identifier 10.1109/TNB.2020.3042266

I. Introduction

TUMOR sensitization and targeting (TST) for early and microscopic tumors remains a big challenge with the constraint of the low resolution of existing medical imaging techniques [1]–[3]. With the development of nanotechnology in the past decades, TST has been provided with many breakthrough solutions. For example, nanoparticles with unique physicochemical properties (i.e., size, shape and surface chemistry) have the ability to detect and kill tumor cells *in vitro* and *in vivo* [4], [5]. The delivery methods of nanoparticles are relying on the organic systemic circulation, which leads to a low delivery ratio of no more than 0.7% as the nanoparticles face both physical and biological barriers once they are injected into the body [6]. Essentially, TST can be seen as a blind path planning problem for drug-loaded vehicles where the target (tumor) position is not known a priori, and various methods for direct manipulation to increase targeting efficiency have been considered [7].

Nanorobotics is a rapidly developing technology by creating robots of nanoscale size with the capabilities

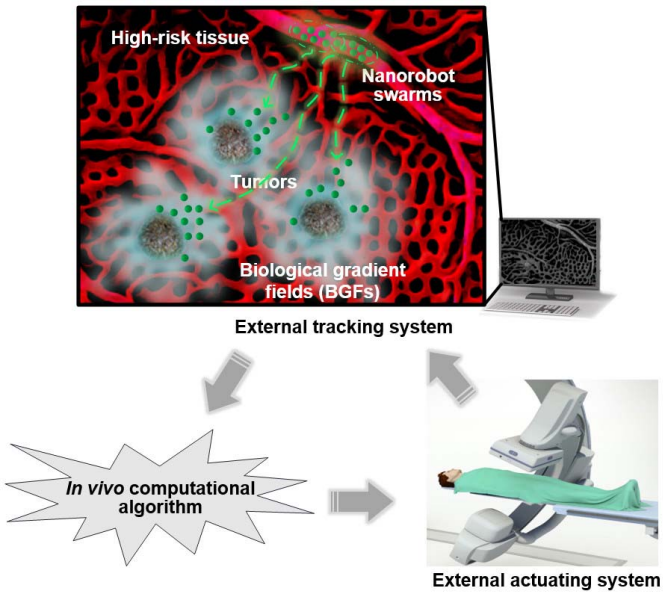

Fig. 1. Nanorobots-assisted natural computation for tumor sensitization and targeting.

of actuating, sensing, information processing, etc., which has the potential to revolutionize current diagnostic and therapeutic techniques in biomedicine [8]–[10]. For example, nanorobots with embedded chemical biosensors can be used to perform detection of tumor in hard-to-reach tissues and human body cavities, which is not possible using current surgical technologies [11]–[14]. Therefore, early detection and localization of solid tumors (e.g., sarcomas, carcinomas, and lymphomas) that may exist in most organs and tissues of the body are considered in this paper.

A. Tumor Sensitization and Targeting as in Vivo Computation

Though the existing research works have shown some positive results of targeted tumor detection and drug delivery, the methodology cannot be applied to an early microscopic tumor, whose location cannot be obtained beforehand due to the resolution limit of the state-of-the-art medical imaging techniques [15]. In other words, the traditional path planning methods cannot be used as they are mainly focusing on the motion control of nanorobots for the detection of a known target point or with a known desirable trajectory [16]–[18]. To address this issue, we have proposed nanorobots-assisted natural computation in our previous investigations, aiming at rendering the TST for early and microscopic tumors into a natural computational process with the consideration of the realistic constraints [19]–[21]. In this way, the process of TST can be interpreted as on-the-fly path planning for nanorobots with unknown tumor positions.

As shown in Fig. 1, externally manipulated nanorobots are utilized as "natural" computing agents in the traditional optimization setting; the tumors targeted are seen as the multiple optimal solutions to be found; the high-risk tissue (the tissue region with likely presence of tumors) is seen as the search space; the tumors-triggered biological gradient fields (BGFs) provide the aided knowledge for fitness evaluation of the nanorobots. The process of nanorobots-assisted TST is similar to the process of solving an optimization problem. Nanorobots are maneuvered by an external actuating device, such as a coil that generates a rotating magnetic field to steer the magnetic nanorobots in fluid, according to the guidance information provided by the swarm intelligence algorithm [22]. Traditional imaging devices can be used as external tracking systems to locate the nanorobots [23]. Meanwhile, the measurable characteristics of nanorobots are obtained during the tracking period, which is used for estimation of the BGF providing the fitness of natural computing agents. It should be noted that the concept of BGF is derived from the biological characteristics of high-risk tissues. For example, the typical skeletonized images of various classes of vascular networks demonstrate that healthy capillaries exhibit almost uniformly distributed grid patterns while the tumor vessels have a profound sort of tortuosity with the density increasing around the tumor [24]. Thus, the measurable characteristics of nanorobots such as trajectories and magnetic changes induced can be used as a BGF for the probe of the host environment with the external tracking system [20].

However, this kind of "natural" computation has some peculiar properties, which distinguish it from traditional optimization and should be taken into account in the process of TST. Firstly, the BGF landscape compensation error should be considered as the nanorobots fabricated with natural materials could cause physical, chemical, and biological interactions with the tissue microenvironment [25], [26]. Secondly, the landscape quantization error caused by the discrete human microvascular network is a basic characteristic of natural computation [27]. Thirdly, the fitness evaluation of computing agents is dependent on the estimation of the BGF landscape by analyzing the measurable characteristics of nanorobots, which is different from the fitness evaluation in traditional optimization without any requirement for on-the-fly estimation [20]. Next, the nanorobots are controlled by the external actuating system with a uniform magnetic field, which means that the other nanorobots will be influenced when one is actuated towards its intended direction [28], [29]. Furthermore, constrained by the control accuracy and imaging resolution of the external devices, the steering and positioning errors in each iteration should be considered [30]. Also, the biochemical reaction between nanorobots and the host environment may lead to their dysfunction, which could result in the finite lifespan of computing agents [31], [32]. Finally, the speeds of nanorobots actuated by an external actuation system are always finite, which is different from the computing agents moving instantaneously in the context of traditional optimization [22].

B. Review of Previous Works

In the process of TST, each computing agent has three operation modes: intended actuating (IA), imaging and tracking (IT), and unintended actuating (UA) with the external devices operating in the time-multiplexed manner [20]. IA / UA is used to actuate the nanorobots by the external actuating system while IT aims at exploiting the BGF estimated from

the nanorobot characteristics measured by an external tracking system. To realize the optimal control of nanorobots in the IA/UA mode with the homogeneous magnetic field generated by the state-of-the-art actuating device, we have proposed a novel evolution strategy, namely the weak priority evolution strategy (WP-ES), which has been used to find an optimal movement direction of nanorobots in each iteration of the swarm intelligence algorithm [29].

Furthermore, to validate the effectiveness of the proposed algorithm for a solitary lesion, we have performed some simulations and *in vitro* experiments in [33]. The Janus particles, which can be controlled *via* a rotating magnetic field, were employed as computing agents in the experiment. A two-dimensional microchannel network fabricated through photolithography was used to represent the vascular network model. Two representative unimodal objective functions were used as the exemplar tumor-triggered BGFs. The experimental results demonstrated the advantages of the proposed targeting strategy on the tumor targeting performance.

C. Contributions of the Current Work

In this article, we focus on the scenario of multifocal tumors, which originate from a unique cellular clone and grow multifocally in a single organ (liver, kidney, thyroid, etc.) [34]. As the targeting strategies proposed in our previous works can only be used in the unifocal case to find an global optimal solution, which does not apply to the multifocal tumors, a new targeting strategy should be proposed. A nanorobot swarm is actuated by a uniform magnetic field to find a tumor focus in an algorithmic cycle, which makes it impossible to complete the TST for multifocal tumors with one nanorobot swarm.

Along this line of thought, we propose a sequential targeting strategy (Se-TS) for multifocal TST, which means a series of nanorobot swarms are employed sequentially in the search space to target the tumors one by one. Specifically, after a tumor is detected by a nanorobot swarm, the BGF landscape of the search space will be modified according to the information gathered during the first TST period. Then, another nanorobot swarm will be employed to detect the second tumor according to the modified landscape. Following this way, all the tumors in the search space should be detected one by one after a pre-specified running time. The optimal paths to reach all the targets can be obtained with all the tumor lesions being detected. Furthermore, the BGFs around all the tumors could be inferred one by one according to the information gathered during the IT periods. This is different from the process of multimodal optimization in traditional optimization context, where the landscapes of multimodal functions cannot be obtained in the searching process. Thus, the Se-TS proposed for multifocal TST is different from the sequential niching method, which is a simple, fast algorithm to identify multiple solutions in a classical multimodal optimization setting.

D. Organization of the Paper

The paper is organized as follows. In Section II, we provide the fundamentals of nanorobots-assisted natural computation for multifocal TST. We then propose the generic Se-TS strategy in Section III and apply it to natural computation algorithms in Section IV. In Section V, we present the nanorobotic experimental platform. In Section VI, we provide *in silico* simulation examples and *in vitro* experiments to demonstrate the effectiveness of the proposed targeting strategy for multifocal TST. Finally, some concluding remarks are drawn in Section VII.

II. Fundamentals of Natural Computation for Multifocal Tumor Sensitization and Targeting

A. Problem Formulation

In the TST process, an external actuating device maneuvers nanorobot swarms to find the tumor lesions according to a specific natural computational algorithm. The tracking system is used to locate the nanorobot swarms and estimate the BGFs according to the measurable characteristics of nanorobots, which are used for the fitness evaluation for the computing agents [19], [29]. In this way, the nanorobots update their locations step by step until the maximum search time is reached.

Based on the analysis above, the optimization problem can be expressed as follows (the minimization operation is used for simplicity and without loss of generality):

$$\boldsymbol{x}^* = \arg\min_{\boldsymbol{x}} U(\boldsymbol{x}; A), \tag{1}$$

where U is an *apparent* objective function representing BGF, which is measured by computing agent A; $\boldsymbol{x} \in \mathbb{S}$ is a bivector representing the possible location of any agent with $\mathbb{S}$ being the search space; $\boldsymbol{x}^*$ represents the locations of the global optimal solutions that remain unchanged regardless of any variation caused by the agents to the BGF landscape.

Furthermore, the *apparent* objective function contains the *true* objective function $U_{\mathrm{T}}(\boldsymbol{x})$ independent of the presence or absence of agent A, the disturbance caused by the agent A to the search space $\mathbb{S}$, and the correction factor accounting for this disturbance as described in [29]. Thus, with the correction factor attempting to counteract the disturbance to minimize its influence on the *true* BGF landscape, the *apparent* objective function is as follows:

$$U(\boldsymbol{x}; A) = U_{\mathrm{T}}(\boldsymbol{x}) + \epsilon(\boldsymbol{x}; A), \tag{2}$$

where $\epsilon(\boldsymbol{x}; A)$ is a random compensation error.

B. Tumor Vascular Network

The nanorobots are controlled by an external actuating device to search for the tumor area in the human microvascular network after they are injected into the high-risk tissue [20]. Thus, the vasculature in the high-risk tissue is the search space $\mathbb{S}$.

The survival and growth of the tumor cells require oxygen and nutrients provided by blood vessels, without which the tumor cannot grow beyond a critical size or metastasize to another organ [35]. In return, the growth of tumor will induce changes to the morphology of capillaries and the characteristics of tumor vascular network will reflect the

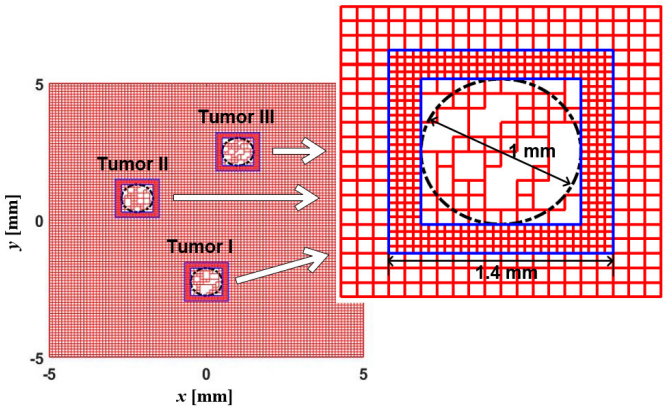

Fig. 2. The microvascular network in the high-risk tissue with the tumor vascular network simulated by invasion percolation algorithm.

changing state of the pathological tissue [36]. Angiogenesis (the formation of new blood vessels) occurs in tumors that have reached 1 to 2 mm in diameter when tumor vessels develop by sprouting or intussusception from pre-existing vessels. As the tumor grows, the vasculature within the core of the tumor will undergo dramatic regression and the center of the tumor will be bereft of vessels gradually. It has been demonstrated that the angiogenesis, vessel cooption (the integration of existing blood vessels into the tumor vasculature), and vessel regression remodel the healthy vascular network into a tumor-specific vasculature, which is bereft of vessels in the center and displays robust angiogenesis around the tumor periphery [35], [37]–[39].

Invasion percolation is an algorithm that models the expansion of a network throughout a medium with randomly distributed heterogeneities in strength, which could properly model the growth procedure of a tumor vascular network [36], [40]. As shown in Fig. 2, three tumor vascular networks in the high-risk tissue are simulated by the invasion percolation algorithm [20], where the black dotted circles with a diameter of 1 mm represent the tumor regions synthesized by the invasion percolation algorithm. The tumor vasculatures are regressed by 40%; the tumor peripheries, where the angiogenesis occurs are represented by the square with a side length of 1.4 mm; the intercapillary distances of healthy tissue and tumor peripheries are set to be 100 μm and 50 μm, respectively, and the search space $\mathbb{S}$ is set to be 10 mm $\times$10 mm.

C. Representative BGF Landscapes

To evaluate the fitness of nanorobots which are natural computing agents during the targeting process, we introduce the concept of BGF, which is derived from the biological characteristics of high-risk tissue regions [29], [33]. For example, the healthy capillaries exhibit almost uniformly distributed grid patterns while the tumor vessels have a profound sort of tortuosity with the density increasing around the lesions; the locations of nanorobots can be estimated through contrast-enhanced medical imaging according to the magnetic response induced by a polarizing magnetic field [41], [42]. Thus, the measurable characteristics of nanorobots (e.g., trajectories, magnetic changes induced) can be used as

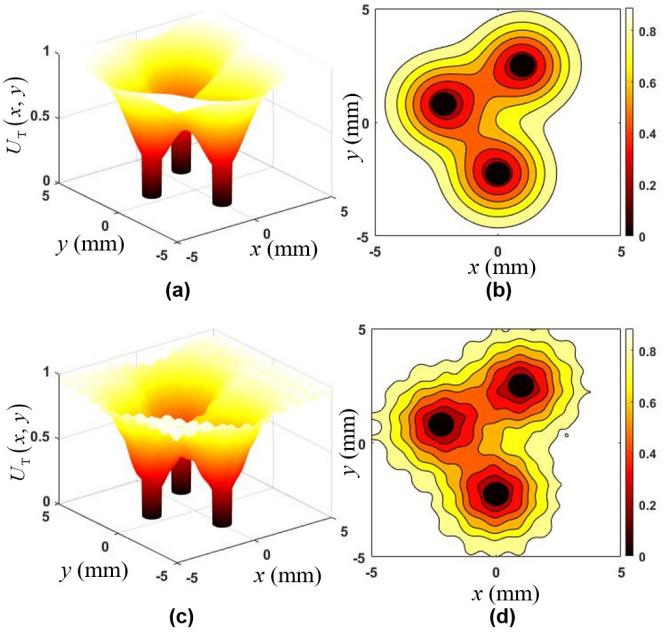

Fig. 3. Illustration of the representative BGF landscapes: (a) Landscape 1 and (b) its contour plot; (c) Landscape 2 and (d) its contour plot.

BGFs for the probe of the host environment with the external monitoring system [20]. Nevertheless, as the research is in its initial stage, there is no widely-accepted, quantitative model on the BGF in the existing literature other than some qualitative observations made from the experimental data.

For illustration purpose, two representative objective functions shown in Fig. 3 are considered in the current work as they could describe the BGFs around the tumors with or without random fluctuations. They are in general agreement with the qualitative observations made in the existing literature and provide some useful insight into the effectiveness of the proposed targeting strategy with varying levels of difficulty depending on the pattern of the gradient. Their arithmetic expressions are shown in (3)-(10). Landscape 1 represents the scenario that BGFs change smoothly around the tumors, while landscape 2 represents more complex BGFs with some fluctuations around the tumors. The circular regions with a radius of 0.5 mm in the center of each BGF represent the tumors targeted. It should be noted that the concept of BGF is different from that of the test function in traditional optimization as the latter represents the integrated characteristic of a problem while the former only represents a biological trait of the high-risk tissue. In this respect, the natural computation is fundamentally different from the traditional optimization framework.

1) Landscape 1:

$$U_{\mathrm{T}}(x,y)=\begin{cases}0, & \sqrt{x^2+(y+2.25)^2}\le 0.5 \text{ and } (x,y)\in\mathbb{S}\\ 0, & \sqrt{(x+2.2)^2+(y-0.8)^2}\le 0.5 \text{ and } (x,y)\in\mathbb{S}\\ 0, & \sqrt{(x-1)^2-(y-2.5)^2}\le 0.5 \text{ and } (x,y)\in\mathbb{S}\\ 1-14/9\pi\,(U_{\mathrm{T1}}(x,y)+U_{\mathrm{T2}}(x,y)+U_{\mathrm{T3}}(x,y)), & \\ \quad \text{Otherwise}, & \end{cases} \tag{3}$$

where,

$$U_{\mathrm{T1}}(x,y)=\exp\left(\left(-x^2-(y+2.25)^2\right)/4.5\right), \tag{4}$$

$$U_{\mathrm{T2}}(x,y)=\exp\left(\left(-(x+2.2)^2-(y-0.8)^2\right)/4.5\right), \tag{5}$$

$$U_{\mathrm{T3}}(x,y)=\exp\left(\left(-(x-1)^2-(y-2.5)^2\right)/4.5\right). \tag{6}$$

2) Landscape 2:

$$U_{\mathrm{T}}(x,y)=\begin{cases}0, & \sqrt{x^2+(y+2.25)^2}\le 0.5 \text{ and } (x,y)\in\mathbb{S}\\ 0, & \sqrt{(x+2.2)^2+(y-0.8)^2}\le 0.5 \text{ and } (x,y)\in\mathbb{S}\\ 0, & \sqrt{(x-1)^2-(y-2.5)^2}\le 0.5 \text{ and } (x,y)\in\mathbb{S}\\ 1-14/9\pi\,(U_{\mathrm{T4}}(x,y)+U_{\mathrm{T5}}(x,y)+U_{\mathrm{T6}}(x,y)), & \\ \quad \text{Otherwise}, & \end{cases} \tag{7}$$

where,

$$\begin{aligned}U_{\mathrm{T4}}(x,y)&=\exp\left(\left(-x^2-(y+2.25)^2\right)/4.5\right)+4.5\pi\\&\quad\times 10^{-4}\left(\cos 2\pi x-\cos\left(2\pi\,(y+2.25)\right)+17\right),\end{aligned} \tag{8}$$

$$\begin{aligned}U_{\mathrm{T5}}(x,y)&=\exp\left(\left(-(x+2.2)^2-(y-0.8)^2\right)/4.5\right)+4.5\pi\\&\quad\times 10^{-4}\left(\cos 2\pi\,(x+2.2)-\cos\left(2\pi\,(y-0.8)\right)+17\right),\end{aligned} \tag{9}$$

$$\begin{aligned}U_{\mathrm{T6}}(x,y)&=\exp\left(\left(-(x-1)^2-(y-2.5)^2\right)/4.5\right)+4.5\pi\\&\quad\times 10^{-4}\left(\cos 2\pi\,(x-1)-\cos\left(2\pi\,(y-2.5)\right)+17\right).\end{aligned} \tag{10}$$

III. Targeting Process for Multifocal Tumors

A. Operation Modes

The search process of nanorobots contains the IT and IA/UA modes, which are implemented with the external tracking and actuating systems in the simple time-multiplexed manner [20], [29]. As the state-of-the-art nanorobotic control technology can only generate a uniform field to maneuver all nanorobots simultaneously, each nanorobot cannot be controlled independently (even in a sequential manner) without affecting others' movement. Thus, any nanorobot working in the IA mode means that the rest would work in the UA mode. As such, IA/UA corresponds to the same duration as shown in Fig. 4(a). Each nanorobot takes turn to operate in the IT and IA/UA modes. For example, agent A_1 works in the IT mode from time $t_{\mathrm{IT},1}$ to $t_{\mathrm{IA},1}$, under the action of the tracking system. During the IT period, A_1 drifts along with the bloodstream, whose flow direction is assumed to be from bottom left to top right in the search space. Thus, A_1 has the same probability to either move up or to the right at each intersection in the vascular network. The location of A_1 is estimated with an error $\Delta\vec{x}_1$, whose horizontal and vertical components are assumed to be independently and identically

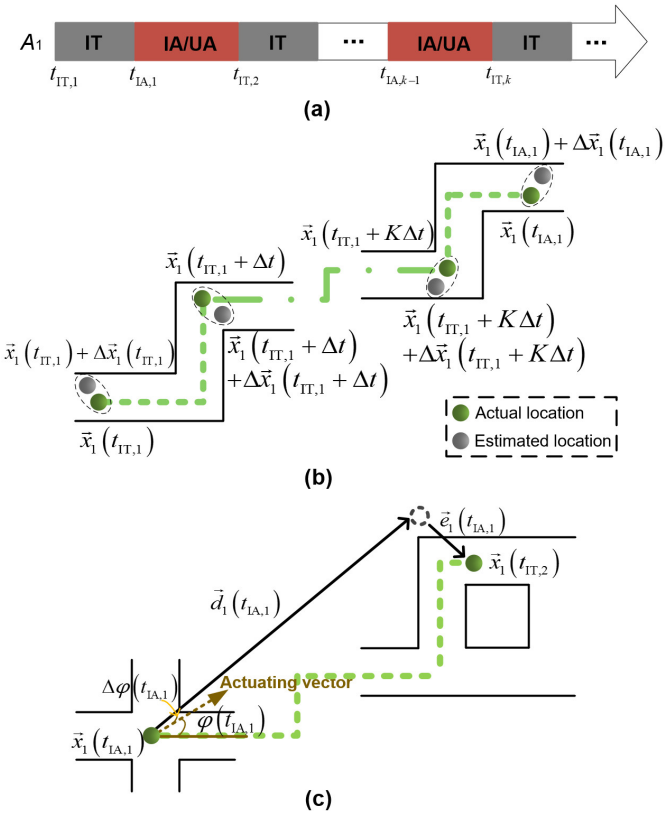

Fig. 4. Operation modes of a nanorobot in the taxicab vascular network: (a) the time sequence of operation modes, (b) the process of IT mode, and (c) the process of IA/UA mode.

distributed Gaussian with variance $\sigma^2_{\Delta x}$ and zero mean for simplicity as shown in Fig. 4(b).

From time $t_{\mathrm{IA},1}$ to $t_{\mathrm{IT},2}$, A_1 operates in the IA/UA mode as shown in Fig. 4(c). During this period, A_1 is propelled by the actuating device along the direction $\varphi\left(t_{\mathrm{IA},1}\right)$ derived from the swarm intelligence algorithm with an angle deviation $\Delta\varphi\left(t_{\mathrm{IA},1}\right)$, which is a random variable summarizing all steering imperfections and is assumed to be normally distributed with variance $\sigma^2_{\Delta\varphi}$ and zero mean. $\vec{e}_1\left(t_{\mathrm{IA},1}\right)$ is the position "quantization" error due to the discrete lattice pattern of the vasculature. Furthermore, $\|\vec{d}_1\left(t_{\mathrm{IA},1}\right)+\vec{e}_1\left(t_{\mathrm{IA},1}\right)\|_1=\|\vec{d}_1\left(t_{\mathrm{IA},1}\right)\|_1$ holds in the vascular network of taxicab geometry.

B. Sequential Targeting Strategy

In traditional mathematical optimization, the sequential niching method is a technique to efficiently locate multiple optimal solutions in multimodal problems [43]. It means that once a potential solution is identified by a specific optimization algorithm, the objective function's fitness landscape will be modified by a derating function at the identified position and the algorithm will be restarted to search for the second solution without converging to the previous one. Iteratively repeating this process a sufficient number of times, as shown in (11), will locate all the global optimal solutions, where $M_n(x,y)$ is the n^{th} modified fitness function, s_n is the n^{th} best individual

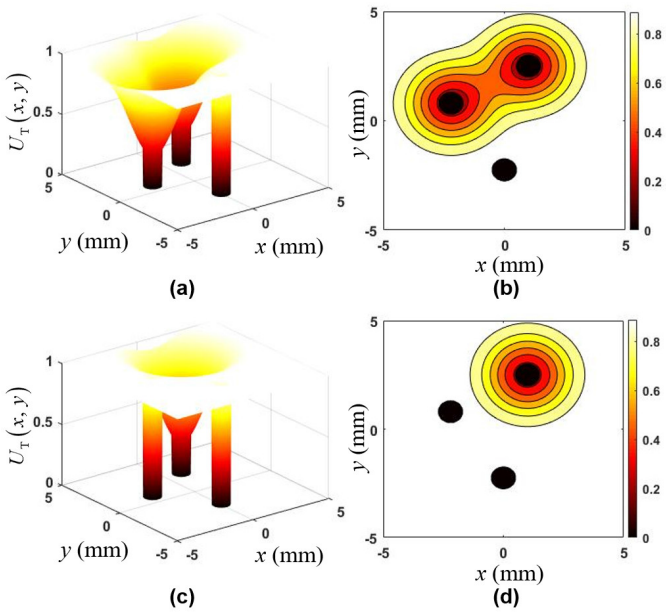

Fig. 5. Transformation results of the BGF landscape: (a) and (b) are the first transformation results, (c) and (d) are the second transformation results.

found, and $G(x, y, s_n)$ is a single-peak derating function [44].

$$M_{n+1}(x, y) = M_n(x, y) * G(x, y, s_n). \tag{11}$$

Inspired by the sequential niching technique, we propose a sequential targeting strategy (Se-TS) for TST. Specifically, the Se-TS contains the following procedures: (1) A swarm of nanorobots are maneuvered by the external actuating and tracking devices according to the WP-ES to find a tumor after they are injected into the high-risk tissue [29]. (2) After the first tumor is detected by the first nanorobot swarm, the BGF landscape is modified according to (12), where $U_{\mathrm{R1}}(x, y)$ is the repair function derived from the estimated local BGF landscape around the tumor detected, and $\delta_1(x, y)$ is a random repair error. After applying the transformation of (12), the new form of the BGF landscape is shown in Fig. 5(a) and (b). Then, the second nanorobot swarm is injected into the high-risk tissue and the search process in (1) is repeated, which will lead to the second tumor being detected. (3) Following this way, the third tumor can be detected by the third nanorobot swarm injected with the BGF landscape being modified according to (13), where $U_{\mathrm{R2}}(x, y)$ is the repair function derived from the estimated local BGF landscape around the second tumor detected, and $\delta_2(x, y)$ is a random repair error. The second transformation results of the BGF landscape are shown in Fig. 5(c) and (d).

$$U'_{\mathrm{T}}(x, y) = U_{\mathrm{T}}(x, y) + U_{\mathrm{R1}}(x, y) + \delta_1(x, y), \tag{12}$$

$$U''_{\mathrm{T}}(x, y) = U'_{\mathrm{T}}(x, y) + U_{\mathrm{R2}}(x, y) + \delta_2(x, y). \tag{13}$$

Different from the traditional sequential niching technique, the repair functions (i.e., $U_{\mathrm{R1}}(x, y)$ and $U_{\mathrm{R2}}(x, y)$) used in the Se-TS are derived according to the local BGF landscapes inferred during the IT periods, which means that the fitness evaluation for the computing agents in TST should be more precise compared to the traditional optimization. Furthermore, the nanorobot swarms are injected sequentially into the high-risk tissue to search for the tumor lesions with different initial times, and this is different from the traditional mathematical optimization with only one population deployed in the search space for the whole optimization procedure.

IV. Sequential Targeting Strategy Based Natural Computational Algorithms

In this section, we introduce the Se-TS into the natural computational algorithms to explore the effect of the proposed targeting strategy for multifocal TST.

A. Se-TS for Gravitational Search Algorithm

The Gravitational search algorithm (GSA) is a stochastic optimization method inspired by the Newtonian gravity and the laws of motion. The computing agents are viewed as objects, whose virtual masses represent their fitness. In the optimization process, the objects tend to attract each other by their virtual gravitational forces. The global movement of all the objects would cause the update of their locations, which corresponds to the candidate solutions of an optimization problem [45].

Considering a system consisting of N agents whose locations are denoted by $\{\vec{x}_1, \vec{x}_2, \cdots, \vec{x}_N\}$, the virtual masses are calculated according to the following equations.

$$\begin{cases} m_i(t) = \dfrac{fit_i(t) - worst(t)}{best(t) - worst(t)} \\ M_i(t) = \dfrac{m_i(t)}{\sum_{j=1}^{N} m_j(t)}, \end{cases} \tag{14}$$

where

$$\begin{cases} best(t) = \max_{i\in 1,2,\cdots,N} fit_i(t) \\ worst(t) = \min_{i\in 1,2,\cdots,N} fit_i(t), \end{cases} \tag{15}$$

with $fit_i(t)$ being the fitness of agent $\vec{x}_i$, whose virtual mass is denoted by $m_i(t)$. The virtual gravitational force acting on agent $\vec{x}_i$ from agent $\vec{x}_j$ is defined as:

$$\vec{F}_{ij} = G(t)\frac{M_i(t) \times M_j(t)}{R_{ij}(t) + \varepsilon}\left(\vec{x}_j(t) - \vec{x}_i(t)\right), \tag{16}$$

with

$$G(t) = G_0 \times \mathrm{e}^{-\alpha t/T}, \tag{17}$$

where $R_{ij}(t)$ is the Euclidean distance between $\vec{x}_i$ and $\vec{x}_j$, ε is a small constant, $G(t)$ denotes a gravitational constant reducing with time, G_0 is set to be 10, α is set to be 5, and T is the maximum iteration number. To obtain a stochastic characteristic, the joint force acting on $\vec{x}_i$ is defined as:

$$\vec{F}_i(t) = \sum_{j=1, j\neq i}^{N} rand_j \vec{F}_{ij}(t), \tag{18}$$

with $rand_j$ being a random number in the interval [0, 1]. Then the acceleration of agent $\vec{x}_i$ at time t is calculated by:

$$\vec{a}_i(t) = \frac{\vec{F}_i(t)}{M_i(t)}. \tag{19}$$

Agent $\vec{x}_i$ updates according to the following equations.

$$\begin{cases} \vec{v}_i\left(t+1\right) = rand_i \cdot \vec{v}_i\left(t\right) + \vec{a}_i\left(t\right) \\ \vec{x}_i\left(t+1\right) = \vec{x}_i\left(t\right) + \vec{v}_i\left(t+1\right). \end{cases} \tag{20}$$

For natural computation, the initial velocities of nanorobots are assumed to be 0 when they are injected into the high-risk tissue as the inertia velocities of nanorobots could be ignored in the bloodstream, which is non-Newtonian liquid. The location update of the computing agents is composed of the IT and IA/UA modes for each iteration as follows.

IT mode:

$$\vec{x}_i\left(t+1\right) = \vec{x}_i\left(t\right) + \mathrm{T}_1 \cdot \vec{v}_b\left(t+1\right), \tag{21}$$

IA/UA mode:

$$\begin{cases} \vec{v}_i\left(t+1\right) = d_0 \cdot \mathrm{e}^{-\kappa \cdot t_{\mathrm{IA},k}/T} \cdot \vec{a}_j\left(t\right) / \|\vec{a}_j\left(t\right)\|_2 \\ \vec{x}_i\left(t+1\right) = \vec{x}_i\left(t\right) + \vec{v}_i\left(t+1\right) + \vec{v}_b\left(t+1\right), \end{cases} \tag{22}$$

where $\vec{v}_b\left(t+1\right)$ is the blood flow velocity at time $(t+1)$, $\vec{a}_j\left(t\right)$ is the acceleration of the selected agent $A_j (j = 1, 2, \cdots, N)$ by WP-ES at time t, T_1 is the IT duration, d_0 is the initial step size, and κ is a small constant.

With the proposed Se-TS introduced into the natural computational algorithm, the pseudo code of the algorithm for multifocal TST is shown in Algorithm 1.

Algorithm 1 Pseudo Code of the GSA Based Multifocal TST Algorithm

```
while the maximum operation time is not reached do
    Generate a new agent swarm in the injection region;
    Evaluate the fitness and lifespan of each agent;
    while the operation time for a tumor targeting is not reached do
        Calculate G(t), best(t), worst(t) and M(t).
        Select the "weakest agent" in the swarm.
        Update according to (21) and (22).
        Evaluate the fitness and lifespan of each agent.
        if any agent reach its lifespan then
            exclude the specific agent from the swarm
        end if
        if any agent reach the tumor region then
            stop its update
        end if
    end while
    Modify the BGF landscape with a specific repair function.
end while
```

B. Se-TS for Particle Swarm Optimization Algorithm

Without loss of generality, we also revisit the particle swarm optimization (PSO), where the optimization process is similar to the behavior of bird flocks and fish schools. The candidate solutions to an optimization problem are assumed as particles that can flow through the search space to achieve the best optimization performance after some iterations. The traditional PSO equations are as follows:

$$\begin{cases} \vec{v}_i\left(t+1\right) = \vec{v}_i\left(t\right) + c_1 \boldsymbol{r}_1 \left(\vec{p}_i - \vec{x}_i\left(t\right)\right) \\ \qquad\qquad + c_2 \boldsymbol{r}_2 \left(\vec{g} - \vec{x}_i\left(t\right)\right) \\ \vec{x}_i\left(t+1\right) = \vec{x}_i\left(t\right) + \vec{v}_i\left(t+1\right), \end{cases} \tag{23}$$

where $\vec{p}_i$ $(i = 1, 2, \cdots, N)$ denotes the "personal best" particle, and $\vec{g}$ is the "global best" of all the particles. c_1 and c_2 are "cognitive coefficient" and "social coefficient", which are used to modulate the magnitude of the steps taken by the particles in the two different directions in the range $0 \le c_1, c_2 \le 4$. $\boldsymbol{r}_1$ and $\boldsymbol{r}_2$ are two diagonal matrices of random numbers generated from a uniform distribution [0, 1]. With the WP-ES being introduced into the PSO, the evolution equations of agents are shown as follows.

IT mode:

$$\vec{x}_i\left(t+1\right) = \vec{x}_i\left(t\right) + \mathrm{T}_1 \cdot \vec{v}_b\left(t+1\right), \tag{24}$$

IA/UA mode:

$$\begin{cases} \vec{v}_i\left(t+1\right) = \vec{v}_i\left(t\right) + c_1 \boldsymbol{r}_1 \left(\vec{p}_i - \vec{x}_i\left(t\right)\right) + c_2 \boldsymbol{r}_2 \left(\vec{g} - \vec{x}_i\left(t\right)\right) \\ \vec{v'}_i\left(t+1\right) = d_0 \cdot \mathrm{e}^{-\kappa \cdot t_{\mathrm{IA},k}/T} \cdot \vec{v}_j\left(t+1\right) / \|\vec{v}_j\left(t+1\right)\|_2 \\ \vec{x}_i\left(t+1\right) = \vec{x}_i\left(t\right) + \vec{v'}_i\left(t+1\right) + \vec{v}_b\left(t+1\right), \end{cases} \tag{25}$$

where $\vec{v}_j\left(t+1\right) / \|\vec{v}_j\left(t+1\right)\|_2$ denotes the moving direction of the particle selected by WP-ES, and the other parameters have the same meanings as those of (22).

The pseudo code of the PSO based natural computational algorithm is shown in Algorithm 2.

Algorithm 2 Pseudo Code of the PSO Based Multifocal TST Algorithm

```
while the maximum operation time is not reached do
    Generate a new agent swarm in the injection region;
    Evaluate the fitness and lifespan of each agent;
    while the operation time for a tumor targeting is not reached do
        Find the "personal best" (p_i) and "global best" (g).
        Select the "weakest particle" in the swarm.
        Update according to (24) and (25).
        Evaluate the fitness and lifespan of each agent.
        if any agent reach its lifespan then
            exclude the specific agent from the swarm
        end if
        if any agent reach the tumor region then
            stop its update
        end if
    end while
    Modify the BGF landscape with a specific repair function.
end while
```

V. Experimental Setup

In order to model the vascular network in the high-risk tissue, we fabricate a two-dimensional microchannel network.

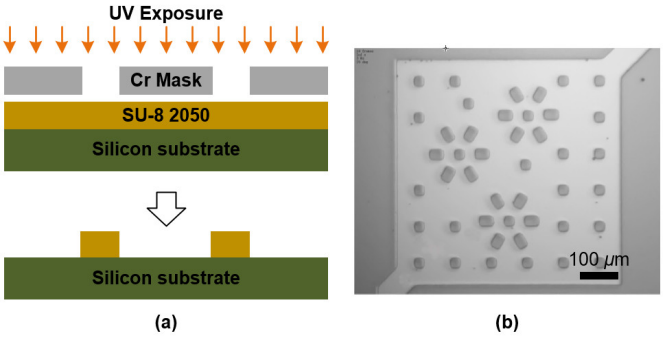

Fig. 6. (a) Schematic diagram of the microfabrication procedure; (b) The vascular network model fabricated.

Fig. 6(a) shows the microfabrication procedure of the microchannel network through photolithography. The silicon substrate covered with a 60 μm layer of SU-8 2050 is exposed under UV lights with a chrome (Cr) mask [33], [46]. The sample of microchannel network developed is shown in Fig. 6(b). Furthermore, to model the heterogeneity of the vessels in the peritumoral areas, the corresponding areas in the microchannel network are set to be denser compared to the other areas.

For the nanorobots used in the experiment, the Janus particles representing the latest effort toward the development of fast, efficient, and controllable fuel-free microdevices were employed [47]. Janus particles were fabricated by half-coating polystyrene (PS) particles 10 μm in diameter with a 100 nm thick layer of nickel (Ni) by electron beam evaporation (Fig. 7(a)). The surface morphology of there Ni-PS particles was confirmed with scanning electron microscopy (SEM) (Fig. 7(b)). Note that although the Janus particles are actually microscale, they are used to represent nanorobots; this is due to the fact that Janus nanoparticles are very difficult to image using our current experimental platform. For translational motion control of the nanorobots, we applied rotating magnetic fields generated by a 3D Helmholtz coil system. The xy motion of the nanorobot was controlled by manipulating the strength (mT), orientation (rad), and frequency (Hz) of the rotating magnetic field. The generated magnetic field can be expressed as

$$\vec{B} = \begin{bmatrix} B_r \sin\theta \cos\omega t \\ B_r \cos\theta \cos\omega t \\ B_r \sin\omega t \end{bmatrix}, \tag{26}$$

where B_r, θ, ω, and t represent the rotating magnetic field, direction of motion, rotational frequency of the field, and time, respectively (Fig. 7(c)).

The nanorobotic control system consists of three pairs of electromagnetic coils arranged in a Helmholtz configuration, three programmable power supplies (Kepco BOP 20-5M), a National Instruments data acquisition (NI DAQ) controller (PCI-6259 and BNC-2110), a microscope, a camera, and a host computer (Fig. 8) [33]. The coil system is powered by the power supplies controlled *via* the DAQ device. The magnetic field generated by per coil pair is around 1.5 mT with a current of 0.45 A. The motion of nanorobots was recorded

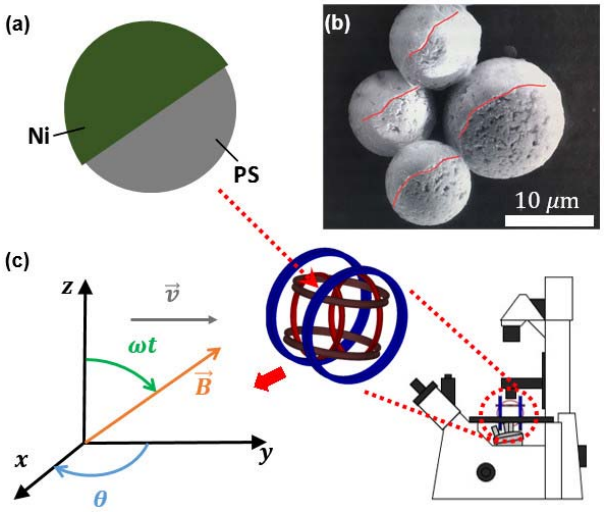

Fig. 7. Schematics of nanorobotic fabrication and control. (a) Illustration of a Janus particle; (b) SEM image of the Janus particles; (c) Schematic of magnetic control.

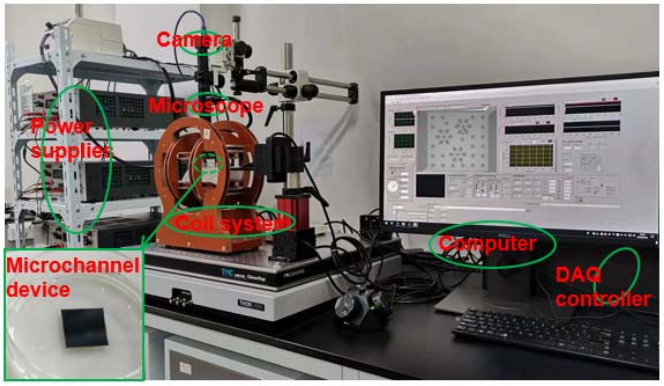

Fig. 8. Experimental platform for *in vivo* computation.

using a CMOS camera (BFS-U3-13Y3M-C) at 25 frames per second with a field of view of 614.4 × 491.5 μm under a 10× objective lens and a resolution of 0.48 μm/pixel. The nanorobots were tracked by real-time image processing with a LabVIEW program developed for the magnetic field controlling.

VI. Performance Analysis

We use several numerical examples to elaborate on the TST performance of the proposed Se-TS for multifocal tumors, which is compared to the brute-force search and the standard swarm intelligence algorithms for the two representative BGF landscapes described in Section II-C.

A. In Silico Simulation Results

In the simulation, 12 agents with lifespans obeying an exponential distribution (i.e., $\tau(A) \sim \text{Exp}(5 \times 10^{-4})$) are employed. The search space $\mathbb{S}$ generated by using the inversion-percolation-based model described in Section II-B is -5 mm $\leq x, y \leq 5$ mm. The nanorobots are uniformly deployed in the initial region $x, y \in [-5, -4]$ when they are

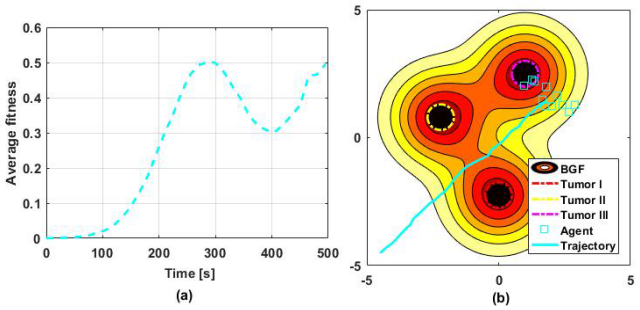

Fig. 9. TST results for landscape 1 by the brute-force search. (a) Average fitness of the agents input during the search time, (b) final locations of the agents input in the search space after one run, and the trajectory of the agent swarm center.

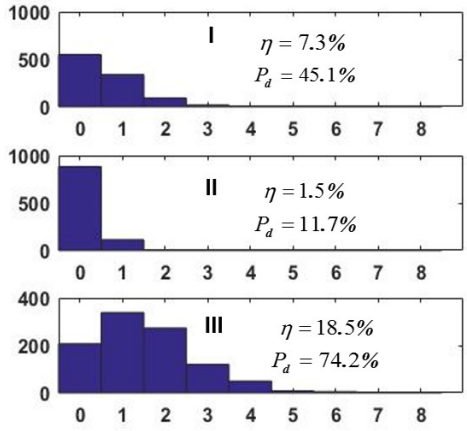

Fig. 10. Histograms of the TST results for the three tumor lesions by using the brute-force search.

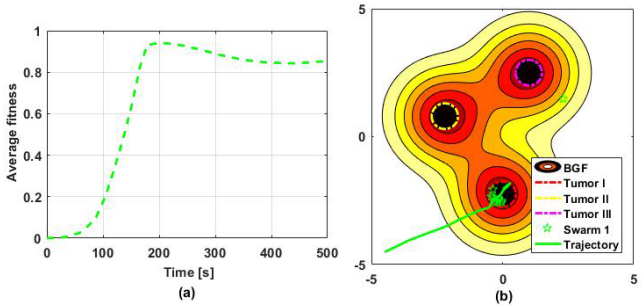

Fig. 11. TST results for landscape 1 by algorithm 1 during the first operation time. (a) Average fitness of the first swarm of agents input, (b) final locations of the agents in the search space, and the trajectory of the first swarm center.

injected into the search space. The speeds of nanorobots and blood flow are set to be 30 μm/s. The direction of blood flow is assumed to be from bottom left to top right of the search space. The duration of IT mode (i.e., T_1) is set to be 10 s. The maximum operation time for the whole search process and the operation time for a tumor targeting are set to be 1500 s and 500 s, respectively. The number of simulation runs is 1000. During the search time, any agent reaching the tumors will stop moving; any agent reaching its lifespan (i.e., the agent dysfunction happens) will be excluded from the swarm with other agents continuing their movement until the operation time is reached. The two representative BGF landscapes are applied to synthesize different levels of multifocal TST difficulty. Three performance metrics P_d, η, and χ are used to represent the ratio of the number of successfully targeted tumors to the total number of simulations, the efficiency of targeting (i.e., the ratio of the amount of agents completing intended tumor targeting to the amount of agents deployed), and the false alarm rate (i.e., the ratio of the amount of agents completing unintended tumor targeting to the amount of agents deployed). η and P_d are used to evaluate the performance of natural computational algorithms compared to the brute-force search from the tumor targeting perspective and the standard swarm intelligence algorithms without any *in vivo* constraints from the algorithmic perspective, while χ is a particular metric for multifocal TST.

Fig. 9 shows the multifocal TST results of the brute-force search for landscape 1, where the agents detect the tumor in the search space $\mathbb{S}$ according to the driving of the blood flow without any aided knowledge from the BGF landscape. The average fitness of agents reaches the two maxima at nearly 300 s and 500 s in this scenario as shown in Fig. 9(a). Fig. 9(b) shows the final locations of the agents in the search space at the search time of 500 s, where we can see only 3 of the 12 agents employed detect the tumor with the rest passing by the tumor regions. To provide better illustration, we present the trajectory of the agent swarm center, from which we can observe that most of the agents miss the tumors with the trajectory passing by the tumors. Furthermore, to provide a quantitative benchmarking scenario, we carried out the simulation for 1000 runs and present the histogram of the results in Fig. 10. It can be seen that the targeting efficiencies for three tumor lesions are 7.3%, 1.5% and 18.5%, and the three targeting ratios are $P_d = 45.1\%$, $P_d = 11.7\%$ and $P_d = 74.2\%$.

To demonstrate the effectiveness of the Se-TS, we carry out the experiment by using three nanorobot swarms to detect the three tumor lesions respectively. The three swarms are injected at 0 s, 500 s, and 1000 s, respectively. Fig. 11(a), Fig. 12 (a) and Fig. 13(a) show the typical curves of the swarms' average fitness over the operation time for landscape 1 by using algorithm 1 in Section IV-A. It shows that the average fitness of the agents reaches the three maxima at around 200 s, 750 s and 1400 s, respectively. Fig. 11(b), Fig. 12(b) and Fig. 13(b) show that most of the agents can detect the three tumor lesions with the trajectories of the swarm centers passing through the tumor regions respectively.

Fig. 14(a) and (b) show the histograms of the multifocal TST results for landscape 1 by using algorithm 1, where $\eta = 41.7\%$, $P_d = 82.4\%$, $\chi = 10.6\%$ for tumor I; $\eta = 50.7\%$, $P_d = 98.4\%$, $\chi = 16.9\%$ for tumor II; and $\eta = 38.1\%$, $P_d = 82.8\%$, $\chi = 12.4\%$ for tumor III. Fig. 15(a) and (b) show the histograms of the multifocal TST results for landscape 2 by using algorithm 1, where $\eta = 38.5\%$, $P_d = 86.9\%$, $\chi = 5.5\%$ for tumor I; $\eta = 26.4\%$, $P_d = 81.3\%$, $\chi = 18.5\%$ for tumor II; and $\eta = 26\%$, $P_d = 69.9\%$, $\chi = 11.8\%$ for tumor III.

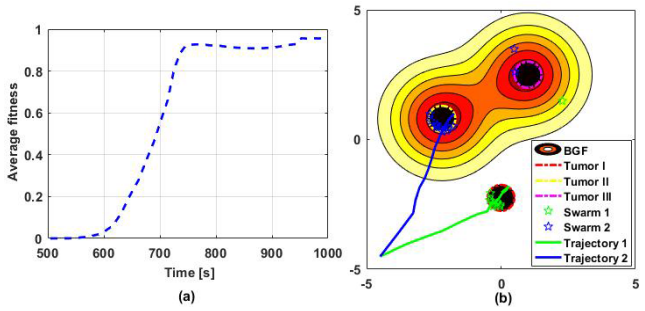

Fig. 12. TST results for landscape 1 by algorithm 1 during the second operation time. (a) Average fitness of the second swarm of agents input, (b) final locations of the agents, and the trajectories of the two swarm centers.

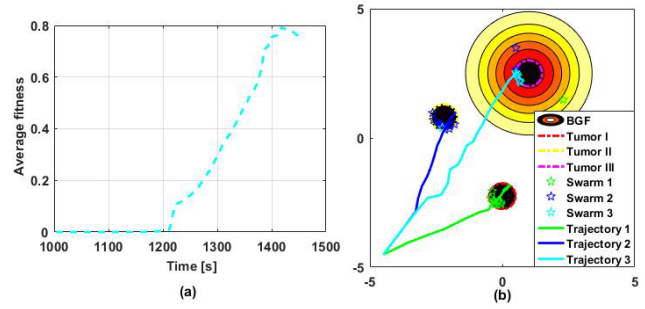

Fig. 13. TST results for landscape 1 by algorithm 1 during the third operation time. (a) Average fitness of the third swarm of agents input, (b) final locations of the agents, and the trajectories of the three swarm centers.

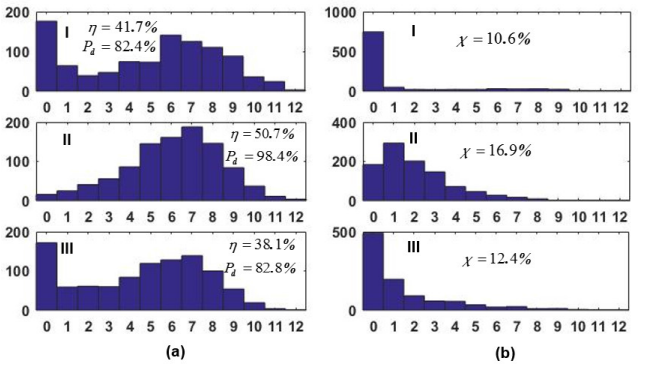

Fig. 14. Histograms of the multifocal TST results for landscape 1 by algorithm 1. (a) Quantity of agents targeting the tumor intended, (b) quantity of agents targeting the tumors unintended.

Furthermore, the multifocal TST results by using algorithm 2 in Section IV-B are similar with that achieved by algorithm 1 shown above. Thus, it is obvious that the Se-TS based natural computational algorithm performs better than the brute-force search from the tumor targeting perspective.

Fig. 16 shows the traditional optimization results for landscape 1 by the sequential niching method based standard GSA. It can be seen that the average fitness of agents reaches the maxima at around the 20^{th}, 40^{th} and 60^{th} iterations, and almost all the agents locate the tumor regions at last. Fig. 17 shows the histograms of the agents locating the tumor regions for landscape 1 and landscape 2.

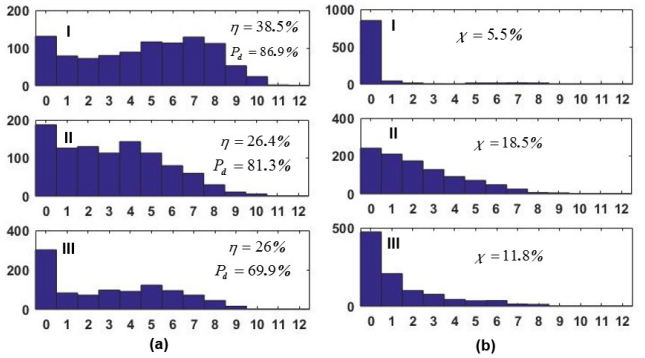

Fig. 15. Histograms of the multifocal TST results for landscape 2 by algorithm 1. (a) Quantity of agents targeting the tumor intended, (b) quantity of agents targeting the tumors unintended.

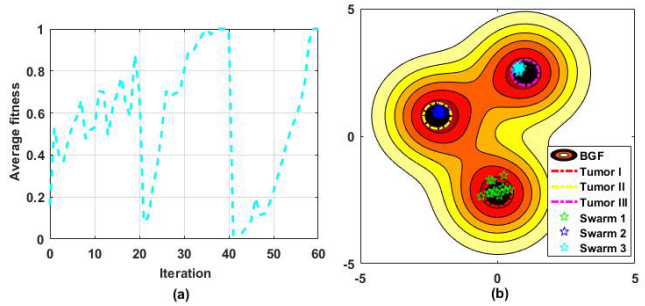

Fig. 16. Multimodal optimization results for landscape 1 by the sequential niching method based standard GSA. (a) Average fitness of the agent swarms input sequentially, (b) final locations of the agents.

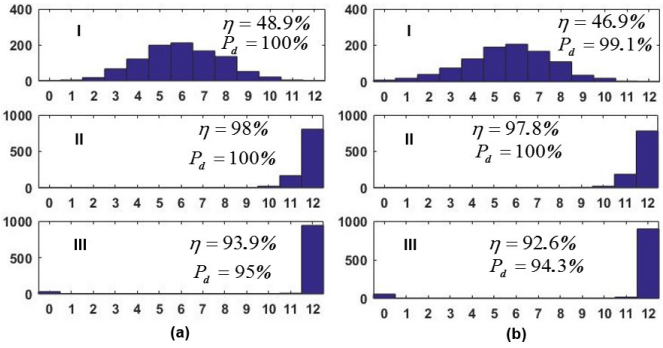

Fig. 17. Histograms of the multimodal optimization results by the sequential niching method based standard GSA. (a) The optimization results for landscape 1, (b) the optimization results for landscape 2.

Thus, we can see that the Se-TS based natural computational algorithms have better multifocal TST performances than the brute-force search, and there is a fundamental distinction between the natural computational algorithms and the standard swarm intelligence algorithms.

B. In Vitro Experimental Results

For the *in vitro* experiment, a group of three Janus particles is used as a nanorobot swarm to detect the tumor regions (i.e., the circular areas with a diameter of 60 μm in the microchannels). The speeds of nanorobots are set to be 5 μm/s. The initial swarm center is at the bottom left corner of the

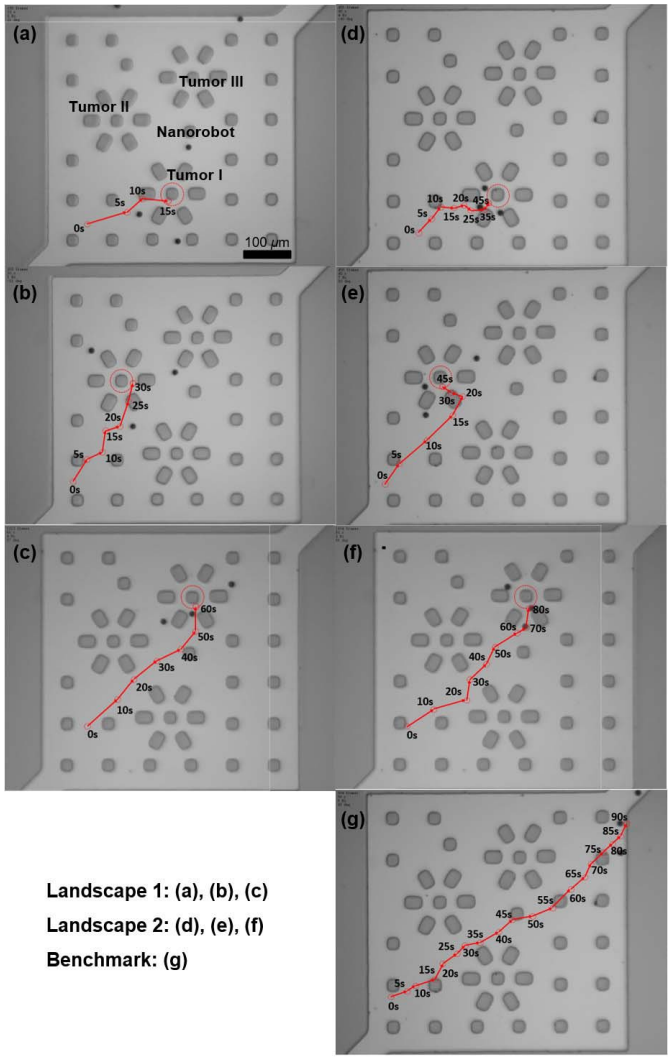

Fig. 18. *In vitro* experimental results for the natural computation.

microchannel network. Fig. 18(a)∼(f) show the trajectories of the swarm centers for landscapes 1 and 2 by using the Se-TS based algorithm. It can be seen that the nanorobot swarms can find the three targets respectively with the operation time elapsing (Supplementary Videos 1-6). As the benchmark scenario, Fig. 18(g) shows the brute-force search result, where we can observe that the nanorobot swarm fails to find the target with the trajectory bypassing the circle regions targeted (Supplementary Video 7).

VII. Conclusion

We proposed the Se-TS for multifocal TST. By introducing the strategy into the natural computational algorithms, we have carried out the *in silico* simulations and *in vitro* experiments for two representative BGF landscapes. The statistical results and *in vitro* validations demonstrate the effectiveness of the proposed strategy.

Future work may include extension of the framework to multi-objective problems and it should be validated by real experiments to justify further its clinical relevance.

References

[1] A. Jemal, F. Bray, M. M. Center, J. Ferlay, E. Ward, and D. Forman, "Global cancer statistics," *CA A, Cancer J. Clinicians*, vol. 61, no. 2, pp. 69–90, Mar. 2011.
[2] A. A. Bharath, "Introductory medical imaging," *Synth. Lectures Biomed. Eng.*, vol. 3, no. 1, pp. 1–186, Jan. 2008.
[3] M. S. Pepe *et al.*, "Phases of biomarker development for early detection of cancer," *J. Nat. Cancer Inst.*, vol. 93, no. 14, pp. 1054–1061, Jul. 2001.
[4] J. D. Kingsley, H. Dou, J. Morehead, B. Rabinow, H. E. Gendelman, and C. J. Destache, "Nanotechnology: A focus on nanoparticles as a drug delivery system," *J. Neuro. Pharm.*, vol. 1, no. 3, pp. 340–350, 2006.
[5] H. Maeda, J. Wu, T. Sawa, Y. Matsumura, and K. Hori, "Tumor vascular permeability and the EPR effect in macromolecular therapeutics: A review," *J. Controlled Release*, vol. 65, nos. 1–2, pp. 271–284, Mar. 2000.
[6] S. Wilhelm *et al.*, "Analysis of nanoparticle delivery to tumours," *Nature Rev. Mater.*, vol. 1, no. 5, p. 16014, May 2016.
[7] M. Arruebo, R. Fernández-Pacheco, M. R. Ibarra, and J. Santamaría, "Magnetic nanoparticles for drug delivery," *Nano Today*, vol. 2, no. 3, pp. 22–32, 2007.
[8] A. Ummat, A. Dubey, and C. Mavroidis, "Bionanorobotics: A field inspired by nature," in *Biomimetics: Biologically Inspired Technologies*. Boca Raton, FL, USA: CRC Press, 2005, pp. 201–227.
[9] V. A. Rahul and G. University, "A brief review on nanorobots," *Int. J. Mech. Eng.*, vol. 4, no. 8, pp. 15–21, Aug. 2017.
[10] T. Nakano *et al.*, "Performance evaluation of leader–follower-based mobile molecular communication networks for target detection applications," *IEEE Trans. Commun.*, vol. 65, no. 2, pp. 663–676, Feb. 2017.
[11] M. Sitti, "Miniature devices: Voyage of the microrobots," *Nature*, vol. 458, no. 7242, p. 1121, 2009.
[12] A. Servant, F. Qiu, M. Mazza, K. Kostarelos, and B. J. Nelson, "Controlled *in vivo* swimming of a swarm of bacteria-like microrobotic flagella," *Adv. Mater.*, vol. 27, no. 19, pp. 2981–2988, May 2015.
[13] O. Felfoul *et al.*, "Magneto-aerotactic bacteria deliver drug-containing nanoliposomes to tumour hypoxic regions," *Nature Nanotechnol.*, vol. 11, no. 11, p. 941, 2016.
[14] J. Li, B. Esteban-Fernández de Ávila, W. Gao, L. Zhang, and J. Wang, "Micro/nanorobots for biomedicine: Delivery, surgery, sensing, and detoxification," *Sci. Robot.*, vol. 2, no. 4, Mar. 2017, Art. no. eaam6431.
[15] A. A. Bui and R. K. Taira, *Medical Imaging Informatics*. Springer, 2009.
[16] S. Chowdhury, W. Jing, P. Jaron, and D. J. Cappelleri, "Path planning and control for autonomous navigation of single and multiple magnetic mobile microrobots," in *Proc. Int. Design Eng. Tech. Conf. Comput. Inf. Eng. Conf.*, 2015, Art. no. V004T09A040.
[17] H. Kim, U. K. Cheang, L. W. Rogowski, and M. J. Kim, "Motion planning of particle based microrobots for static obstacle avoidance," *J. Micro-Bio Robot.*, vol. 14, nos. 1–2, pp. 41–49, Jun. 2018.
[18] T. Xu, J. Yu, X. Yan, H. Choi, and L. Zhang, "Magnetic actuation based motion control for microrobots: An overview," *Micromachines*, vol. 6, no. 9, pp. 1346–1364, Sep. 2015.
[19] Y. Chen, S. Shi, X. Yao, and T. Nakano, "Touchable computing: Computing-inspired bio-detection," *IEEE Trans. Nanobiosci.*, vol. 16, no. 8, pp. 810–821, Dec. 2017.
[20] Y. Chen, M. Ali, S. Shi, and U. K. Cheang, "Biosensing-by-learning direct targeting strategy for enhanced tumor sensitization," *IEEE Trans. Nanobiosci.*, vol. 18, no. 3, pp. 498–509, Jul. 2019.
[21] S. Shi, N. Sharifi, U. K. Cheang, and Y. Chen, "Perspective: Computational nanobiosensing," *IEEE Trans. Nanobiosci.*, vol. 19, no. 2, pp. 267–269, Apr. 2020.
[22] J. Ali *et al.*, "Fabrication and magnetic control of alginate-based rolling microrobots," *AIP Adv.*, vol. 6, no. 12, Dec. 2016, Art. no. 125205.
[23] X. Yan *et al.*, "Multifunctional biohybrid magnetite microrobots for imaging-guided therapy," *Sci. Robot.*, vol. 2, no. 12, Nov. 2017, Art. no. eaaq1155.
[24] Y. Gazit, D. A. Berk, M. Leunig, L. T. Baxter, and R. K. Jain, "Scale-invariant behavior and vascular network formation in normal and tumor tissue," *Phys. Rev. Lett.*, vol. 75, no. 12, pp. 2428–2431, Sep. 1995.
[25] S. Kim, S. Lee, J. Lee, B. J. Nelson, L. Zhang, and H. Choi, "Fabrication and manipulation of ciliary microrobots with non-reciprocal magnetic actuation," *Sci. Rep.*, vol. 6, no. 1, p. 30713, Nov. 2016.
[26] Y. Chen, T. Nakano, P. Kosmas, C. Yuen, A. V. Vasilakos, and M. Asvial, "Green touchable nanorobotic sensor networks," *IEEE Commun. Mag.*, vol. 54, no. 11, pp. 136–142, Nov. 2016.

[27] M. Sefidgar *et al.*, "Numerical modeling of drug delivery in a dynamic solid tumor microvasculature," *Microvascular Res.*, vol. 99, pp. 43–56, May 2015.
[28] U. K. Cheang and M. J. Kim, "Self-assembly of robotic micro- and nanoswimmers using magnetic nanoparticles," *J. Nanoparticle Res.*, vol. 17, no. 3, p. 145, Mar. 2015.
[29] S. Shi, Y. Chen, X. Yao, and M. Zhang, "Lightweight evolution strategies for nanoswimmers-oriented *in vivo* computation," in *Proc. IEEE Congr. Evol. Comput. (CEC)*, Jun. 2019, pp. 866–872.
[30] U. K. Cheang, H. Kim, D. Milutinović, J. Choi, and M. J. Kim, "Feedback control of an achiral robotic microswimmer," *J. Bionic Eng.*, vol. 14, no. 2, pp. 245–259, Jun. 2017.
[31] J. Wong, A. Chilkoti, and V. T. Moy, "Direct force measurements of the streptavidin–biotin interaction," *Biomolecular Eng.*, vol. 16, nos. 1–4, pp. 45–55, Dec. 1999.
[32] U. Kei Cheang, K. Lee, A. A. Julius, and M. J. Kim, "Multiple-robot drug delivery strategy through coordinated teams of microswimmers," *Appl. Phys. Lett.*, vol. 105, no. 8, Aug. 2014, Art. no. 083705.
[33] S. Shi *et al.*, "Microrobots based *in vivo* evolutionary computation in two-dimensional microchannel network," *IEEE Trans. Nanotechnol.*, vol. 19, pp. 71–75, 2020.
[34] W. A. Berg and P. L. Gilbreath, "Multicentric and multifocal cancer: Whole-breast US in preoperative evaluation," *Radiology*, vol. 214, no. 1, pp. 59–66, Jan. 2000.
[35] P. Carmeliet and R. K. Jain, "Angiogenesis in cancer and other diseases," *Nature*, vol. 407, no. 6801, pp. 249–257, Sep. 2000.
[36] Y. Gazit, J. W. Baish, N. Safabakhsh, M. Leunig, L. T. Baxter, and R. K. Jain, "Fractal characteristics of tumor vascular architecture during tumor growth and regression," *Microcirculation*, vol. 4, no. 4, pp. 395–402, Jan. 1997.
[37] J. Holash, "Vessel cooption, regression, and growth in tumors mediated by angiopoietins and VEGF," *Science*, vol. 284, no. 5422, pp. 1994–1998, Jun. 1999.
[38] J. W. Baish and R. K. Jain, "Fractals and cancer," *Cancer Res.*, vol. 60, no. 14, pp. 3683–3688, 2000.
[39] H. Rieger and M. Welter, "Integrative models of vascular remodeling during tumor growth," *Wiley Interdiscipl. Rev., Syst. Biol. Med.*, vol. 7, no. 3, pp. 113–129, May 2015.
[40] J. W. Baish, Y. Gazit, D. A. Berk, M. Nozue, L. T. Baxter, and R. K. Jain, "Role of tumor vascular architecture in nutrient and drug delivery: An invasion percolation-based network model," *Microvascular Res.*, vol. 51, no. 3, pp. 327–346, May 1996.
[41] O. M. Bucci *et al.*, "Experimental framework for magnetic nanoparticles enhanced breast cancer microwave imaging," *IEEE Access*, vol. 5, pp. 16332–16340, 2017.
[42] O. M. Bucci, L. Crocco, and R. Scapaticci, "On the optimal measurement configuration for magnetic nanoparticles-enhanced breast cancer microwave imaging," *IEEE Trans. Biomed. Eng.*, vol. 62, no. 2, pp. 407–414, Feb. 2015.
[43] X. Li, "Developing niching algorithms in particle swarm optimization," in *Handbook of Swarm Intelligence*. Berlin, Germany: Springer, 2011.
[44] D. Beasley, D. R. Bull, and R. R. Martin, "A sequential niche technique for multimodal function optimization," *Evol. Comput.*, vol. 1, no. 2, pp. 101–125, Jun. 1993.
[45] E. Rashedi, H. Nezamabadi-pour, and S. Saryazdi, "GSA: A gravitational search algorithm," *Inf. Sci.*, vol. 179, no. 13, pp. 2232–2248, Jun. 2009.
[46] H. Kim, U. K. Cheang, D. Kim, J. Ali, and M. J. Kim, "Hydrodynamics of a self-actuated bacterial carpet using microscale particle image velocimetry," *Biomicrofluidics*, vol. 9, no. 2, Mar. 2015, Art. no. 024121.
[47] T. Li *et al.*, "Janus microdimer surface walkers propelled by oscillating magnetic fields," *Adv. Funct. Mater.*, vol. 28, no. 25, 2018, Art. no. 1706066.